Available online at www.sciencedirect.com
ScienceDirect
Trans. Nonferrous Met. Soc. China 35(2025) 2666−2682
Transactions of Nonferrous Metals Society of China
www.tnmsc.cn

Phase equilibria and wear mechanism of Cu−Zr−Si alloys

Ben-fu LI[1], Biao HU[1], Xin-yue HUANG[1], Rui ZUO[1],
Yu-ling LIU[1], Xin-yue LAN[1], Liang-yan HAO[2], Wei XIONG[2], Rong-xun PIAO[3]

1. School of Materials Science and Engineering, Anhui University of Science and Technology, Huainan 232001, China;
2. Department of Mechanical Engineering and Materials Science, University of Pittsburgh, Pittsburgh 15261, USA;
3. School of Mechanical Engineering, Anhui University of Science and Technology, Huainan 232001, China

Received 17 November 2023; accepted 6 August 2024

Abstract: The phase equilibria of the Cu−Zr−Si system at 600 °C were experimentally studied by means of X-ray diffraction (XRD) and scanning electron microscopy with energy dispersive X-ray spectroscopy (SEM−EDS). A comprehensive set of thermodynamic parameters for the Cu−Zr−Si system were obtained through detailed analysis using the CALPHAD (CALculation of PHAse Diagrams) approach. Based on the CALPHAD calculations, five as-cast alloys were designed, and the Scheil−Gulliver model was used to simulate their solidification paths. By testing hardness, friction and wear properties, the wear resistance of the Cu−Zr−Si alloys was investigated. Wear morphologies were analyzed using SEM and 3D profiling techniques. It was found that the alloy $Cu_{80}Zr_{19}Si_1$ exhibits a good performance with a hardness of HV 342, frictional coefficient of 0.23 and wear rate of 2.19×10^{-7} mm^3/(N·m). The wear surfaces are mainly characterized by grooves, spalling pits and oxide particles. The wear mechanism of the alloys is adhesive wear and oxidative wear under dry sliding condition. This study provides a theoretical basis for the design of the wear-resistant Cu−Zr−Si alloys.

Key words: Cu−Zr−Si alloy; thermodynamic modeling; CALPHAD approach; friction coefficient; wear mechanism

1 Introduction

Copper (Cu) alloys are widely utilized as wear-resistant materials due to their good mechanical and wear-resistant properties [1−3]. Currently, the mass production of wear resistant Cu alloys includes aluminum bronze, tin bronze and silicon bronze. They are used in the automotive, machinery and aerospace industries to produce parts such as bearings and worm gears [4]. Due to the increasingly complex and demanding service environment, higher requirements for the properties of Cu alloys have been put forward. The addition of appropriate trace alloying elements, such as Zr [5] and Si [6], can improve the mechanical properties and wear resistance of Cu alloys [7,8]. For example, the experimental results from DONG et al [9] indicate that the tensile strength of the Cu−0.15Zr−0.05Si (wt.%) alloy after cold deformation and aging can exceed 400 MPa, and the maximum microhardness is approximately HV 150. LI et al [10] investigated the friction and wear behavior of Cu−0.1Zr (wt.%) alloys and found that the alloys obtained by equal-channel angular pressing (ECAP) have higher wear resistance due to grain refinement. However, most of the available studies focused on the effect of trace amounts of Zr and Si on the mechanical performance of Cu alloys. The present work aims to investigate the friction and wear behavior of the Cu alloys containing high contents of Zr and Si with the guidance of the CALPHAD

Corresponding author: Biao HU, Tel/Fax: +86-554-6634027, E-mail: hubiao05047071@163.com
https://doi.org/10.1016/S1003-6326(25)66839-7

approach [11], which is an effective computational tool widely employed for alloy design.

A thorough understanding of the phase equilibria for the Cu−Zr−Si system is critical to the design of new Cu alloys. Two teams of researchers have investigated the phase equilibria of the Cu−Zr−Si system at 800 °C [12], 750 °C and 900 °C [13]. To provide more experimental data for thermodynamic modeling, the isothermal section of the Cu−Zr−Si system at 600 °C was investigated by key experiments in the present work. A set of thermodynamic parameters of the Cu−Zr−Si system were then obtained using the CALPHAD method. Afterwards, five compositions of the Cu−Zr−Si alloys were selected according to the thermodynamic calculations to investigate their friction and wear properties. Meanwhile, their microstructures were analyzed by SEM−EDS, and the solidification behaviors under non-equilibrium conditions were simulated by the Scheil−Gulliver model.

2 Research methods

2.1 Experimental procedures

High-purity Cu (99.99 wt.%), Si (99.99 wt.%), and Zr (99.99 wt.%) (China New Metal Materials Technology Co., Ltd.) were used as raw materials. The Cu−Zr−Si alloys were prepared in a non-consumable vacuum arc melter (WK-I, Physcience Opto-electronics Co., Ltd., China). The alloys tested for phase equilibria were placed in vacuum quartz tubes and annealed at 600 °C for 60 d using a chamber furnace (KSL−1200X, Hefei Kejing Material Technology Co., Ltd., China).

XRD patterns of the alloys were examined using Cu K_α radiation at 40 kV and 300 mA (Smartlab SE, Rigaku Corporation, Japan). The scanning rate was 5 (°)/min and the diffraction patterns were obtained in the 2θ range of 20°−80°. The surface morphology and wear morphology of the alloys were observed using SEM (MIRA4, TESCAN, Czech Republic) with an accelerating voltage of 30 kV. The phase compositions of the alloys were examined by EDS.

2.2 Thermodynamic models

The Gibbs energy functions of the pure elements Cu, Zr and Si were taken from the SGTE database compiled by DINSDALE [14]. The thermodynamic parameters of the Cu−Zr, Cu−Si and Si−Zr binary systems reported by LIU et al [15], YAN and CHANG [16], and GUENEAU et al [17], respectively, were accepted in the present work. The calculated binary phase diagrams are shown in Fig. 1. The crystal structure information for all solid phases in the Cu−Zr−Si system is listed in Table 1.

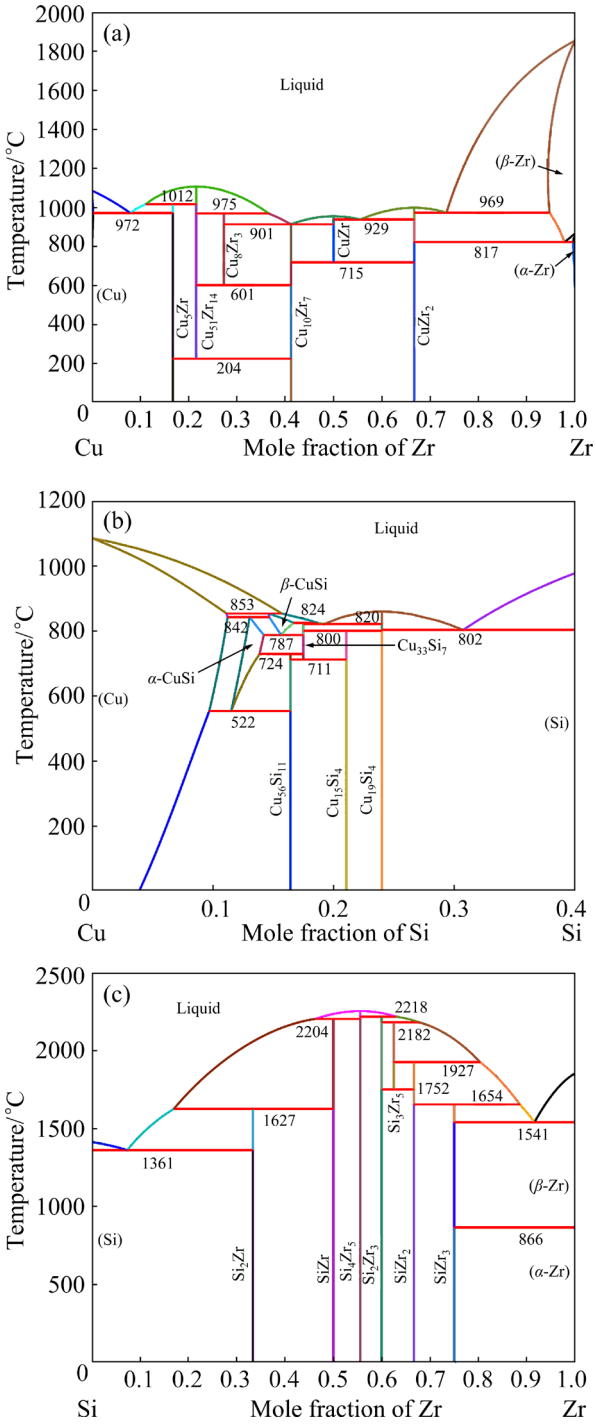

Fig. 1 Calculated Cu−Zr (a), Cu−Si (b) and Si−Zr (c) phase diagrams using thermodynamic parameters from LIU et al [15], YAN and CHANG [16], and GUENEAU et al [17], respectively

Table 1 Crystal structures of solid phases in Cu–Zr–Si system

Phase	Space group	Pearson symbol	Prototype	Lattice parameter/nm		
				a	*b*	*c*
(Cu)	$Fm\bar{3}m$	*cF*4	Cu	0.3615	0.3615	0.3615
(Si)	$Fd\bar{3}m$	*cF*8	C	0.5430	0.5430	0.5430
(α-Zr)	$P6_3/mmc$	*hP*2	Mg	0.3232	0.3232	0.5148
(β-Zr)	$Im\bar{3}m$	*cI*2	W	0.3309	0.3309	0.3309
CuZr	$Pm\bar{3}m$	*cP*2	CsCl	0.3259	0.3259	0.3259
$CuZr_2$	*I*4/*mmm*	*tI*6	$MoSi_2$	0.3220	0.3220	1.1183
Cu_5Zr	*P*4/*m*	*tP*24	–	0.6856	0.6856	0.6882
$Cu_{51}Zr_{14}$	*P*6/*m*	*hP*65	$Ag_{51}Gd_{14}$	1.1244	1.1244	0.8282
Cu_8Zr_3	*Pnma*	*oP*44	Cu_8Hf_3	0.7869	0.8155	0.9985
$Cu_{10}Zr_7$	*C*2*ca*	*oC*68	$Ni_{10}Zr_7$	1.2673	0.9316	0.9347
$Cu_{19}Si_6$	$R\bar{3}m$	*hR*∗	–	0.6038	0.6369	0.4286
$Cu_{15}Si_4$	$I\bar{4}3d$	*cI*76	–	0.9731	0.9731	0.9731
$Cu_{56}Si_{11}$	$P4_132$	*cP*20	–	0.6232	0.6232	0.6232
$Cu_{33}Si_7$	–	*t*∗∗	–	0.8815	0.8815	0.7903
α-CuSi	$P6_3/mmc$	*hP*2	Mg	2.5610	2.5610	4.1840
β-CuSi	$Im\bar{3}m$	*cI*2	W	–	–	–
α-SiZr	*Pnma*	*oP*8	FeB	0.6982	0.3786	0.5302
β-SiZr	*Cmcm*	*oC*8	CrB	0.3764	0.9917	0.3748
Si_2Zr	*Cmcm*	*oC*12	$ZrSi_2$	0.3696	0.1475	0.3665
α-Si_4Zr_5	$P4_12_12$	*tP*36	Zr_5Si_4	0.7123	0.7123	1.3002
β-Si_4Zr_5	*Pnma*	*oP*36	Ge_4Sm_5	0.6949	1.3588	0.7109
Si_2Zr_3	*P*4/*mbm*	*tP*10	U_3Si_2	0.7082	0.7082	0.3714
$SiZr_2$	*I*4/*mcm*	*tI*12	Al_2Cu	0.6612	0.6612	0.5294
Si_3Zr_5	$P6_3/mcm$	*hP*16	Mn_5Si_3	0.7914	0.7914	0.5559
$SiZr_3$	$P4_2/n$	*tP*32	Ti_3P	1.1011	1.1011	0.5453
$CuZr_2Si_4$	*Cmcm*	–	$CuGe_4Hf_2$	0.3681	0.3704	3.2910
$CuZrSi_2$	*P*4/*nmm*	*tP*8	–	0.3724	0.3724	0.9029
τ_1 ($Cu_4Zr_3Si_6$)	*I*4/*mmm*	*tI*26	$Cu_4Si_6Zr_3$	0.3736	0.3736	2.8186
τ_2 ($Cu_4Zr_3Si_4$)	*Immm*	*oI*22	$Cu_8Ge_8Gd_6$	1.3090	0.6393	0.3934
τ_3 (CuZrSi)	*Pbnm*	–	Co_2Si	0.6506	0.3921	0.7278
τ_4 ($Cu_4Zr_3Si_2$)	$P\bar{6}3n$	*hP*9	Fe_2P	0.6372	0.6372	0.3890

The solution phases, i.e., liquid, (Cu), (Zr) and (Si), were described by the substitutional solution model. The excessive Gibbs energy of mixing was expressed by the Redlich−Kister−Muggianu polynomial [18]. The binary and ternary interaction parameters can be expressed as $L=A+BT$, where L is the interaction parameter, T is the thermodynamic temperature. The coefficients A and B were optimized based on the experimental data. The detailed description can be found elsewhere [19−21]. According to the experimental observation in the present work and literature [12,13], Si_2Zr, Si_4Zr_5, Si_2Zr_3, $SiZr_3$, $SiZr_2$ and Si_3Zr_5 phases can dissolve a certain amount of Cu, whereas the solubilities of the

third element in $Cu_{19}Si_6$, $Cu_{15}Si_4$, α-CuSi, $Cu_{56}Si_{11}$, $CuZr_2$, $Cu_{10}Zr_7$, Cu_5Zr and $Cu_{51}Zr_{14}$ phases are negligible.

Ternary compounds $\tau_1(Cu_4Zr_3Si_6)$, $\tau_2(Cu_4Zr_3Si_4)$, τ_3(CuZrSi) and $\tau_4(Cu_4Zr_3Si_2)$ were treated as stoichiometric based on the experimental results from the present work, SPRENGER [12] and XIAO et al [13].

2.3 Tribological tests

The surface of the samples was polished to remove the surface impurities and the oxide layer before testing. The hardness tests were carried out using a Vickers hardness tester (HV−30Z, Shuangli Instrument Technology Co., Ltd., China) on the mechanically polished samples with a load of 1 kg and a holding time of 10 s. The average of five measured values was taken as the hardness value of each sample. The Vickers hardness (HV) of the alloy was calculated by

$$\mathrm{HV}=\frac{2F\sin(136°/2)}{d^2}\approx 0.189\frac{F}{d^2} \quad (1)$$

where the indenter angle is 136°, F is the test force, and d is the arithmetic mean of the two diagonals. The schematic diagram of the Vickers hardness test is shown in Fig. 2(a).

The friction and wear experimental studies of the as-cast alloys were performed on a pin-disk wear and friction tester (MPX−3G, Jinan Puye Electromechanical Technology Co., Ltd., China). The schematic diagram of the friction and wear testing machine is shown in Fig. 2(b). The carbon steel was used as the friction sub-fitting for the friction test, with a speed of 200 r/min, a load of 100 N, and a friction time of 300 s. The surface of samples needs to be polished to a roughness (R_a) of less than 0.5 μm before testing. The wear rate (W) was calculated according to the wear formula [8,22]:

$$W=\frac{m_1-m_2}{2\pi Rtn\rho F} \quad (2)$$

where m_1 and m_2 are the masses before and after wear (mg), R is the friction radius (R=15 mm), t is the friction time (s), n is the rotational speed (r/min), ρ is the density of alloys B1−B5, and F is the normal force applied to the sample (N). The morphological characteristics of the samples wear surface were investigated and analyzed by SEM−EDS and 3D Profiling (PS50, NANOVEA, USA).

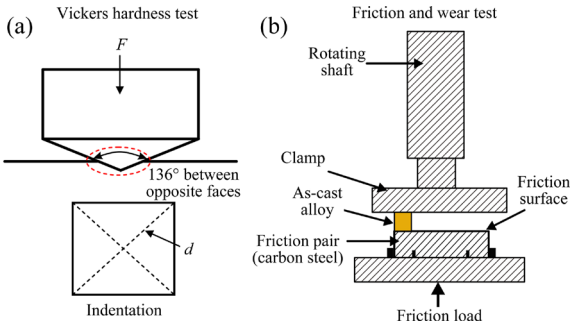

Fig. 2 Schematic diagrams for Vickers hardness (a), and friction and wear (b) tests

3 Results and discussion

3.1 Phase equilibria at 600 °C

Sixteen annealed alloys were prepared to investigate the phase equilibria of the Cu−Zr−Si system at 600 °C. The phases identified by XRD and their compositions measured by SEM−EDS are summarized in Table 2.

The XRD patterns and scanning electron microscopy (SEM) images of four representative alloys are shown in Fig. 3. For Alloy A1, Fig. 3(a) reveals three phases with grey, dark grey and black contrasts. These phases τ_1, Si_2Zr and (Si) are confirmed by the XRD pattern, as shown in Fig. 3(b). Combining the results of XRD and SEM−EDS, Alloy A1 is located in a three-phase region, i.e., τ_1+Si_2Zr+(Si). Figure 3(c) shows three contrasts, i.e., grey, dark grey and black, which correspond to τ_1, $Cu_{19}Si_6$ and (Si), respectively, in Alloy A2, which are also detected by XRD, as indicated in Fig. 3(d). Thus, Alloy A2 is located in a three-phase region, i.e., τ_1+$Cu_{19}Si_6$+(Si). The composition of the ternary phase τ_1 is determined to be $Cu_{32.5}Zr_{22.6}Si_{44.9}$ (at.%). According to the EDS results, the solubilities of Cu and Zr in (Si) are less than 1 at.%. The SEM micrograph and XRD pattern of Alloy A3 are shown in Figs. 3(e) and (f), respectively. Based on the SEM−EDS results, the grey, dark grey and black regions correspond to SiZr, τ_1 and Si_2Zr, respectively. Their characteristic diffraction peaks are also observed in the XRD pattern. The XRD and SEM−EDS results confirm that Alloy A3 is located in a three-phase region, i.e., τ_1+SiZr+Si_2Zr. As revealed by the SEM micrograph in Fig. 3(g), Alloy A5 consists of the Si_2Zr_3, Si_4Zr_5 and τ_3 phases, which demonstrate the light grey, grey and dark grey contrasts, respectively. That is

Table 2 Summary of identified phases and their compositions by XRD and SEM−EDS

Alloy	Nominal composition	Phase	Content/at.%		
			Cu	Zr	Si
A1	$Cu_{5.62}Si_{69.04}Zr_{25.34}$	(Si)	0.3	0.6	99.1
		Si_2Zr	0.7	34.0	65.3
		τ_1	31.0	23.3	45.7
A2	$Cu_{38.41}Si_{53.38}Zr_{8.21}$	(Si)	0.9	0.2	98.9
		$Cu_{19}Si_6$	72.1	0.4	27.5
		τ_1	32.5	22.6	44.9
A3	$Cu_{24.19}Si_{47.15}Zr_{28.66}$	SiZr	1.5	50.9	47.6
		Si_2Zr	3.5	33.6	62.9
		τ_1	31.5	23.8	44.7
A4	$Cu_{32.83}Si_{37.72}Zr_{29.45}$	SiZr	3.7	50.3	46.0
		τ_1	33.1	23.7	43.2
		τ_2	37.2	27.7	35.1
A5	$Cu_{10.36}Si_{39.06}Zr_{50.58}$	Si_2Zr_3	3.9	60.7	35.4
		Si_4Zr_5	1.0	57.2	41.8
		τ_3	34.2	34.7	31.1
A6	$Cu_{43.53}Si_{30.96}Zr_{25.51}$	τ_3	34.7	33.2	32.1
		τ_2	39.3	27.0	33.7
A7	$Cu_{74.71}Si_{23.93}Zr_{1.36}$	$Cu_{15}Si_4$	79.5	0.0	20.5
		τ_1	33.2	23.3	43.5
		τ_2	40.9	24.8	34.3
A8	$Cu_{32.52}Si_{29.72}Zr_{37.76}$	Si_2Zr_3	0.9	63.8	35.3
		τ_3	35.4	33.5	31.1
		τ_4	41.5	35.0	23.5
A9	$Cu_{26.66}Si_{13.7}Zr_{59.64}$	$SiZr_2$	2.1	65.5	32.4
		$CuZr_2$	34.9	65.1	0.0
		$Cu_{10}Zr_7$	54.2	45.6	0.2
A10	$Cu_{84.69}Si_{12.9}Zr_{2.41}$	(Zr)	1.1	98.2	0.7
		$CuZr_2$	33.6	66.4	0.0
		$SiZr_3$	2.6	74.9	22.5
A11	$Cu_{81.3}Si_{4.39}Zr_{13.81}$	(Cu)	99.1	0.8	0.1
		Cu_5Zr	81.1	18.9	0.0
		τ_3	36.3	33.6	30.1
A12	$Cu_{76.01}Si_{18.07}Zr_{5.91}$	α-CuSi	88.0	0.2	11.8
		$Cu_{56}Si_{11}$	84.4	0.2	15.4
		τ_2	37.4	27.6	35.0
A13	$Cu_{54.38}Si_{13.1}Zr_{13.52}$	Si_2Zr_3	4.5	61.4	34.1
		$Cu_{51}Zr_{14}$	77.9	22.0	0.1
		τ_4	46.5	33.7	19.8
A14	$Cu_{38.9}Si_{14.4}Zr_{46.7}$	Si_2Zr_3	6.1	60.4	33.5
		$Cu_{10}Zr_7$	58.8	41.2	0.0
		$Cu_{51}Zr_{14}$	78.0	21.4	0.6
A15	$Cu_{76.77}Si_{2.71}Zr_{20.53}$	$Cu_{51}Zr_{14}$	78.6	21.3	0.1
		Cu_5Zr	82.0	18.0	0.0
A16	$Cu_{79.80}Si_{19.03}Zr_{1.17}$	$Cu_{15}Si_4$	78.3	0.3	21.4
		$Cu_{56}Si_{11}$	83.6	0.0	16.4
		τ_2	40.3	25.9	33.8

confirmed by XRD, as shown in Fig. 3(h). The solubilities of Cu in the Si_2Zr_3 and Si_4Zr_5 phases are about 3.9 at.% and 1.0 at.%, respectively. The composition of the ternary phase τ_3 is 34.2 at.% Cu, 34.7 at.% Zr and 31.1 at.% Si.

Based on the experimental analysis, 14 three-phase regions, i.e., τ_1+Si_2Zr+(Si), τ_1+$Cu_{19}Si_6$+(Si), τ_1+Si_2Zr+SiZr, τ_1+τ_2+SiZr, τ_3+Si_2Zr_3+Si_4Zr_5, τ_1+τ_2+$Cu_{15}Si_4$, τ_3+τ_4+Si_2Zr_3, $SiZr_2$+$CuZr_2$+$Cu_{10}Zr_7$, (Zr)+$CuZr_2$+$SiZr_3$, τ_3+(Cu)+Cu_5Zr, α-CuSi+$Cu_{56}Si_{11}$+τ_2, Si_2Zr_3+$Cu_{51}Zr_{14}$+τ_4, Si_2Zr_3+$Cu_{10}Zr_7$+$Cu_{51}Zr_{14}$ and $Cu_{15}Si_4$+$Cu_{56}Si_{11}$+τ_2, and two two-phase regions, i.e., τ_2+τ_3 and Cu_5Zr+$Cu_{51}Zr_{14}$, are determined at 600 °C. Based on the phases identified in Alloys A9 and A10 and the Gibbs phase rule, a three-phase region $SiZr_2$+$SiZr_3$+$CuZr_2$ can be deduced. Similarly, four three-phase regions $Cu_{19}Si_6$+$Cu_{15}Si_4$+τ_1, CuSi+(Cu)+τ_2, (Cu)+τ_2+τ_3 and $SiZr_2$+Si_2Zr_3+$Cu_{10}Zr_7$ can also be deduced.

3.2 Thermodynamic calculation

Considering both the experimental findings from the present investigation and pertinent literature [23,24], the thermodynamic parameters of the Cu−Zr−Si system were optimized using the PARROT module of the Thermo-Calc software. The step-by-step optimization procedure [19,20,25] was utilized in the present assessment. The optimization starts with the isothermal section at 600 °C. The temperature-independent coefficient A of the ternary interaction parameters was calculated using the phase equilibria data and Cu solubilities in binary compounds, namely Si_2Zr, Si_4Zr_5, Si_2Zr_3, $SiZr_2$, $SiZr_3$ and Si_3Zr_5. The corresponding temperature-dependent coefficient B was obtained from the isothermal sections at 750, 800 and 900 °C. The optimized thermodynamic parameters are listed in Table 3.

Figure 4 shows the calculated isothermal sections at 600, 750, 800 and 900 °C of the Cu−Zr−Si system along with the experimental data from the present work, SPRENGER [12] and XIAO et al [13]. As can be seen, most of the experimental data can be well reproduced by the present calculation. For the isothermal section at 600 °C shown in Fig. 4(a), 23 three-phase regions are predicted, which is in agreement with the experimental results. In the present work, the solubilities of Zr and Si in the Cu–Si and Cu–Zr binary compounds are ignored. The calculated

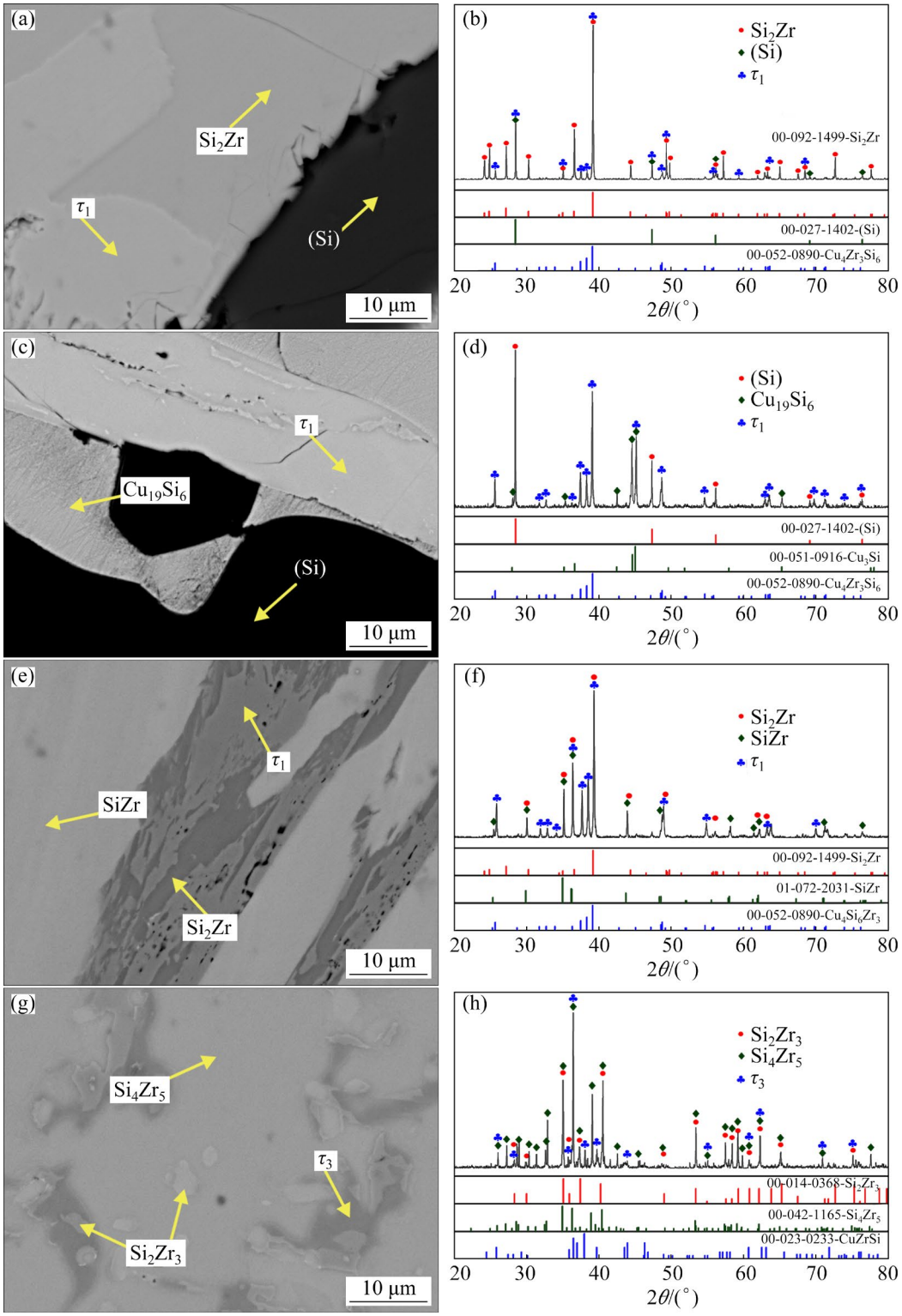

Fig. 3 SEM micrographs and XRD patterns of representative alloys annealed at 600 °C for 60 d: (a, b) Alloy A1 ($Cu_{5.62}Si_{69.04}Zr_{25.34}$); (c, d) Alloy A2 ($Cu_{38.41}Si_{53.38}Zr_{8.21}$); (e, f) Alloy A3 ($Cu_{24.19}Si_{47.15}Zr_{28.66}$); (g, h) Alloy A5 ($Cu_{10.36}Si_{39.06}Zr_{50.58}$)

solubilities of Cu in the $SiZr_3$, $SiZr_2$, Si_2Zr_3, SiZr and Si_2Zr phases are 3.0 at.%, 1.6 at.%, 4.0 at.%, 2.0 at.% and 3.4 at.%, respectively. Figures 4(b) and (d) compare the calculated isothermal sections at 750 and 900 °C, respectively, with the experimental ones by XIAO et al [13]. Figure 4(c) presents the calculated isothermal section at 800 °C compared with the experimental data by SPRENGER [12]. It is found that the calculated phase equilibria among the Si_2Zr, τ_1 and SiZr phases are inconsistent with

Table 3 Obtained thermodynamic parameters of Cu–Zr–Si system

Phase	Model	Gibbs free energy/(J·mol^{-1})
SiZr	$(Cu,Si)_1Zr_1$	${}^{\Theta}G^{SiZr}_{Cu:Zr} = 4967 + {}^{\Theta}G^{fcc}_{Cu} + {}^{\Theta}G^{hcp}_{Zr}$ ${}^{\Theta}G^{SiZr}_{Cu,Si:Zr} = -167760 + 56.45T$
Si_2Zr	$(Cu,Si)_2Zr_1$	${}^{\Theta}G^{Si_2Zr}_{Cu:Zr} = -29603 + 2{}^{\Theta}G^{fcc}_{Cu} + {}^{\Theta}G^{hcp}_{Zr}$ ${}^{\Theta}G^{Si_2Zr}_{Cu,Si:Zr} = -154704$
Si_4Zr_5	$(Cu,Si)_4Zr_5$	${}^{\Theta}G^{Si_4Zr_5}_{Cu:Zr} = -20360 + 4{}^{\Theta}G^{fcc}_{Cu} + 5{}^{\Theta}G^{hcp}_{Zr}$ ${}^{\Theta}G^{Si_4Zr_5}_{Cu,Si:Zr} = -10000$
Si_2Zr_3	$(Cu,Si)_2Zr_3$	${}^{\Theta}G^{Si_2Zr_3}_{Cu:Zr} = 1000 + 2{}^{\Theta}G^{fcc}_{Cu} + 3{}^{\Theta}G^{hcp}_{Zr}$ ${}^{\Theta}G^{Si_2Zr_3}_{Cu,Si:Zr} = -128210 + 66.66T$
$SiZr_2$	$(Cu,Si)_1Zr_2$	${}^{\Theta}G^{SiZr_2}_{Cu:Zr} = -10084 + {}^{\Theta}G^{fcc}_{Cu} + 2{}^{\Theta}G^{hcp}_{Zr}$ ${}^{\Theta}G^{Si_2Zr_3}_{Cu,Si:Zr} = -39623 + 33.84T$
$SiZr_3$	$(Cu,Si)_1Zr_3$	${}^{\Theta}G^{SiZr_3}_{Cu:Zr} = -10047 + {}^{\Theta}G^{fcc}_{Cu} + 3{}^{\Theta}G^{hcp}_{Zr}$ ${}^{\Theta}G^{SiZr_3}_{Cu,Si:Zr} = -77575 + 66T$
τ_1	$Cu_4Zr_3Si_6$	${}^{\Theta}G^{Cu_4Zr_3Si_6}_{Cu:Zr:Si} = -625253 + 4{}^{\Theta}G^{fcc}_{Cu} + 3{}^{\Theta}G^{hcp}_{Zr} + 6{}^{\Theta}G^{diamond}_{Si}$
τ_2	$Cu_4Zr_3Si_4$	${}^{\Theta}G^{Cu_4Zr_3Si_4}_{Cu:Zr:Si} = -600000 + 4{}^{\Theta}G^{fcc}_{Cu} + 3{}^{\Theta}G^{hcp}_{Zr} + 4{}^{\Theta}G^{diamond}_{Si}$
τ_3	$Cu_1Zr_1Si_1$	${}^{\Theta}G^{CuZrSi}_{Cu:Zr:Si} = -184500 + {}^{\Theta}G^{fcc}_{Cu} + {}^{\Theta}G^{hcp}_{Zr} + {}^{\Theta}G^{diamond}_{Si}$
τ_4	$Cu_4Zr_3Si_2$	${}^{\Theta}G^{Cu_4Zr_3Si_2}_{Cu:Zr:Si} = -423000 + 4{}^{\Theta}G^{fcc}_{Cu} + 3{}^{\Theta}G^{hcp}_{Zr} + 2{}^{\Theta}G^{diamond}_{Si}$

T is the thermodynamic temperature (K)

those reported by XIAO et al [13]. In the present work, the phases in Alloy A3 are SiZr, Si_2Zr and τ_1. The experimental phase regions of $Si_2Zr+\tau_1+\tau_2$ reported by XIAO et al [13] and SPRENGER [12] are consistent.

3.3 Solidification microstructure and Scheil simulation

To investigate the effect of different phases on the wear resistance of the Cu−Zr−Si alloys, five alloys with varying contents of Zr and Si were selected from different regions on the vertical section at 80 at.% Cu, which was calculated using the thermodynamic parameters obtained in the present work. The microstructures of these alloys were analyzed by SEM−EDS and the measured phase compositions are summarized in Table 4.

The BSE micrograph of Alloy B1 is shown in Fig. 5(a), which presents two different contrasts, i.e., white and light grey. According to the EDS results, they correspond to τ_3 and $Cu_{33}Si_7$, respectively. In the enlarged micrograph (Fig. 5(b)), the dark grey $Cu_{19}Si_6$ phase and σ with the peritectic structure are detected. The composition of σ is $Cu_{46.1}Zr_{22.5}Si_{31.4}$ (at.%). The corresponding elemental mapping graphs indicate that Zr is mainly distributed in the ternary compounds, while Cu and Si are evenly distributed in the entire microstructure. The micrograph of Alloy B2 in Fig. 5(c) shows the white, grey and dark grey contrasts, which present the τ_3, β-CuSi and α-CuSi phases, respectively. The σ phase is detected in the enlarged micrograph as shown in Fig. 5(d). From the SEM images and EDS analysis, the as-cast Alloys B3−B5 consist of (Cu)+β-CuSi+τ_3, Cu_5Zr+(Cu)+τ_3, and $Cu_{51}Zr_{14}$+(Cu), respectively.

Based on the obtained thermodynamic parameters of the Cu−Zr−Si system in the present work, the calculated solidification curves and step diagrams for the designed alloys are shown in Fig. 6. According to Fig. 6(a), the solidification path of Alloy B1 is as follows: Liquid → Liquid + τ_3 → Liquid + τ_2 → Liquid + τ_2 + $Cu_{33}Si_7$ → Liquid + τ_2 + $Cu_{19}Si_6$ + $Cu_{33}Si_7$. The solidification path shows that the primary crystallization phase of Alloy B1 is τ_3. Afterwards, Alloy B1 undergoes a peritectic reaction, i.e., Liquid + τ_3 → τ_2. The $Cu_{33}Si_7$ phase is formed at about 825 °C, followed by the $Cu_{19}Si_6$ phase. The final solidification microstructure for Alloy B1 is composed of $Cu_{19}Si_6$, $Cu_{33}Si_7$ and τ_2, which is inconsistent with the experimental observation ($Cu_{19}Si_6$ + $Cu_{33}Si_7$ + τ_3). That is due to the small amount of τ_2, which is difficult to be detected by SEM. Furthermore, Fig. 6(b) reveals

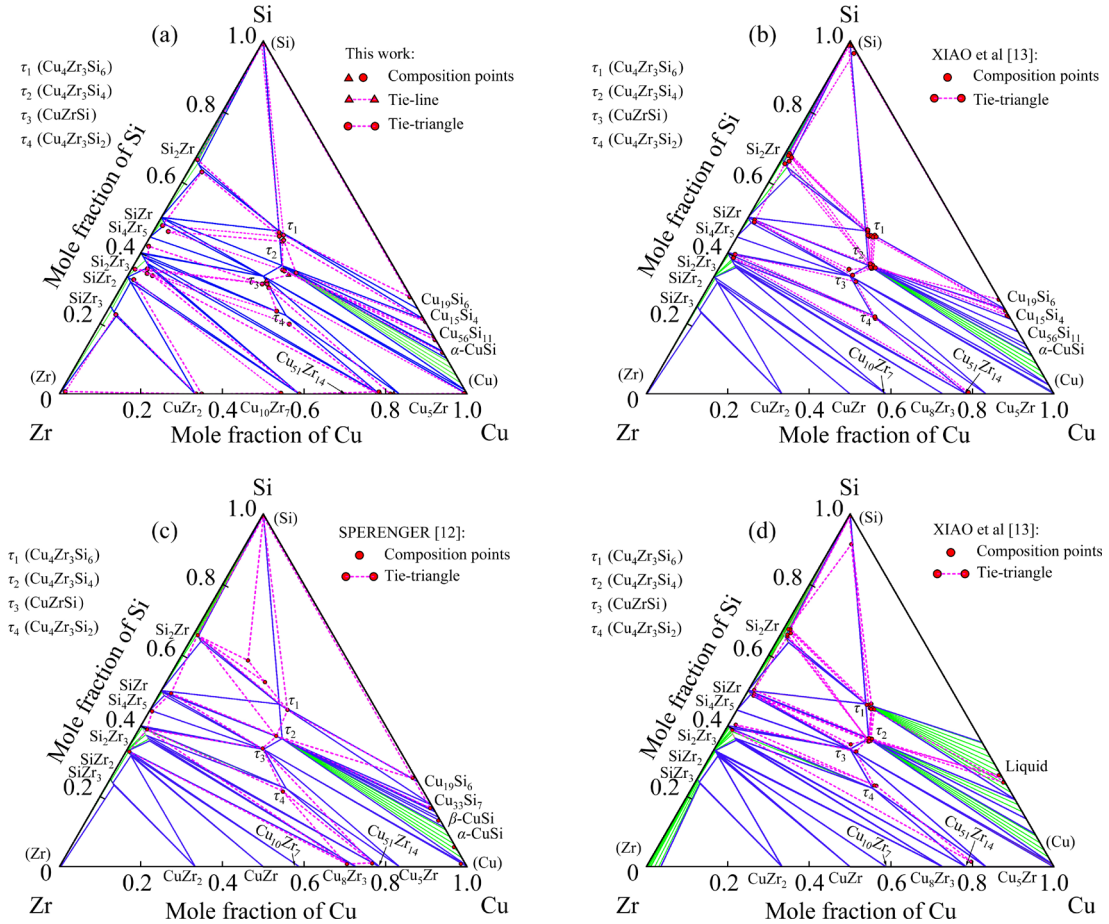

Fig. 4 Calculated isothermal sections of Cu−Zr−Si system according to experimental data of this work, SPERENGER [12] and XIAO et al [13]: (a) 600 °C (This work); (b) 750 °C [13]; (c) 800 °C [12]; (d) 900 °C [13]

Table 4 Phase compositions of as-cast alloys determined by SEM−EDS

Alloy	Nominal composition	Phase	Content/at.%		
			Cu	Zr	Si
B1	$Cu_{80}Zr_1Si_{19}$	τ_3	37.4	32.4	30.2
		$Cu_{33}Si_7$	82.8	0.2	17.0
		$Cu_{19}Si_6$	80.2	0.1	19.7
		σ	46.1	22.5	31.4
B2	$Cu_{80}Zr_4Si_{16}$	τ_3	36.4	32.3	31.3
		α-CuSi	86.5	0.2	13.3
		β-CuSi	83.6	0.1	16.3
		σ	46.3	26.2	27.5
B3	$Cu_{80}Zr_8Si_{12}$	τ_3	36.2	32.4	31.4
		(Cu)	92.4	0.2	7.4
		β-CuSi	83.0	5.89	11.1
		σ	40.2	30.3	29.5
B4	$Cu_{80}Zr_{13}Si_7$	τ_3	36.2	32.7	31.1
		(Cu)	98.9	0.5	0.6
		Cu_5Zr	85.1	14.6	0.3
B5	$Cu_{80}Zr_{19}Si_1$	(Cu)	99.5	0.2	0.3
		$Cu_{51}Zr_{14}$	77.2	22.0	0.8

that the $Cu_{33}Si_7$ and $Cu_{19}Si_6$ phases are formed from the liquid phase at almost identical temperatures with the phase fractions of 0.818 and 0.161, respectively. Figure 6(c) shows the solidification path for Alloy B2 is as follows: Liquid → Liquid + τ_3 → Liquid + τ_2 → Liquid + τ_2 + α-CuSi → Liquid + τ_2 + α-CuSi+ β-CuSi. Similarly, the primary crystallization phase is τ_3. As the temperature decreases, the τ_2 phase solidifies. Alloy B2 then undergoes an invariant reaction, i.e., Liquid + τ_2 → τ_2 + α-CuSi. The α-CuSi phase solidifies at about 880 °C, followed by the formation of the β-CuSi phase at 850 °C. At the solidus temperature of 820 °C, the final solidification microstructure consists of α-CuSi + β-CuSi + τ_3 + τ_2, in which the phase fraction of the τ_2 phase is approximately 0.2 at.%, as shown in Fig. 6(d). By comparing the phase fractions in Alloys B1 and B2, it can be found that Alloy B1 contains more τ_2 than Alloy B2.

The solidification path (Fig. 6(e)) of Alloy B3 is as follows: Liquid → Liquid + τ_3 → Liquid + τ_3 +

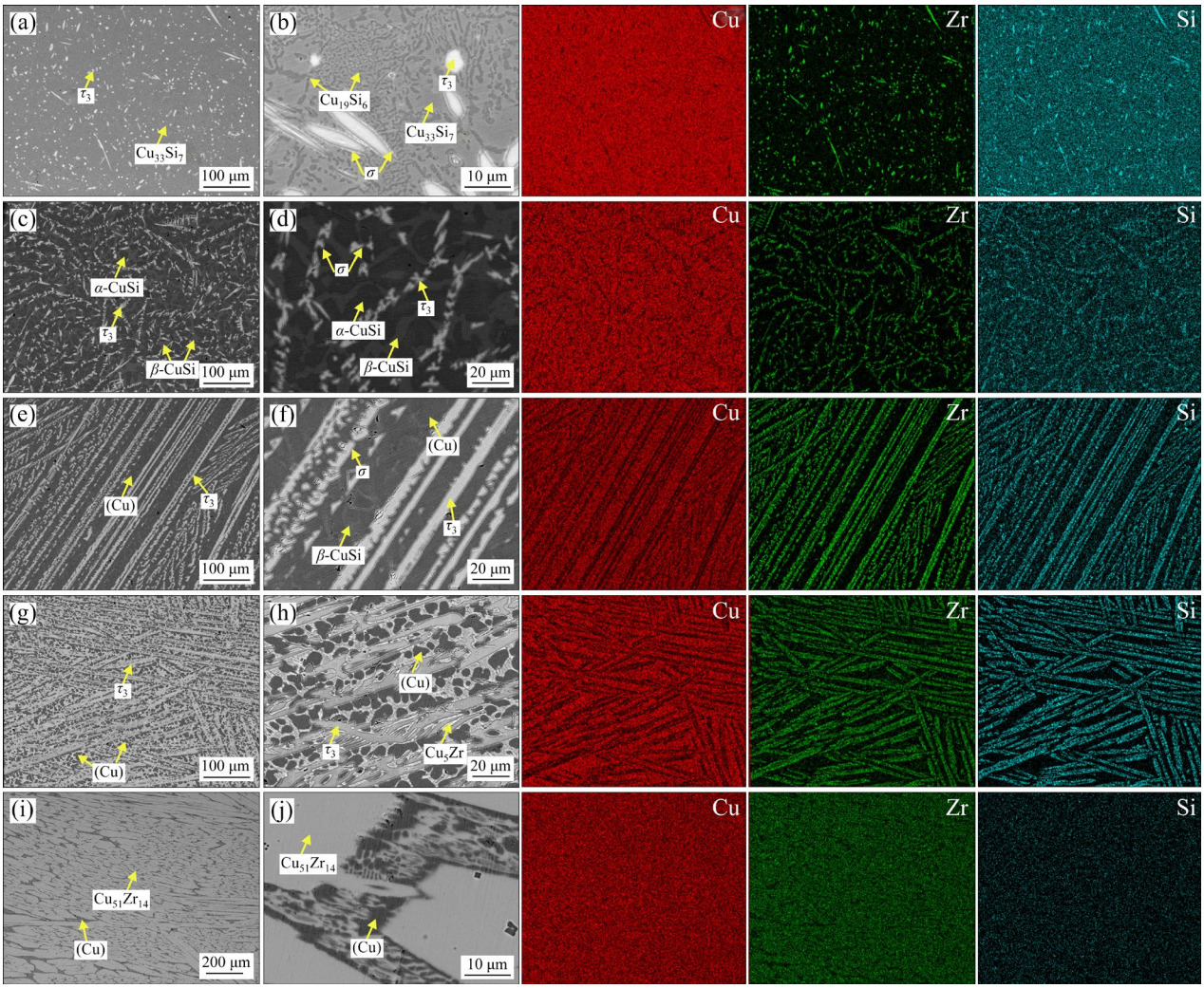

Fig. 5 BSE micrographs and elemental mappings of different alloys: (a, b) Alloy B1 ($Cu_{80}Zr_1Si_{19}$); (c, d) Alloy B2 ($Cu_{80}Zr_4Si_{16}$); (e, f) Alloy B3 ($Cu_{80}Zr_8Si_{12}$); (g, h) Alloy B4 ($Cu_{80}Zr_{13}Si_7$); (i, j) Alloy B5 ($Cu_{80}Zr_{19}Si_1$) (For each alloy, the first micrograph shows the solidified microstructure, the second micrograph is an enlargement of the first one, and the third to fifth micrographs next are elemental mappings for Cu, Zr and Si, respectively)

(Cu) → Liquid + τ_2 + (Cu) → Liquid + τ_2 + (Cu) + β-CuSi. Based on the phase fraction vs temperature curve for Alloy B3, the phase fractions of β-CuSi and τ_2 are 2.5×10^{-3} at.% and 7.3×10^{-3} at.%, respectively. According to the solidification curve of Alloy B4 in Fig. 6(g), its solidification path is as follows: Liquid → Liquid + τ_3 → Liquid + τ_3 + (Cu) → Liquid + τ_3 + (Cu) + Cu_5Zr. The primary crystallization phase is τ_3 formed at 2000 °C. With the decrease of the temperature, the (Cu) phase solidifies at about 970 °C, and finally Cu_5Zr solidifies. The final microstructure Cu_5Zr + (Cu) + τ_3 is consistent with the experimental results. In Fig. 6(h), both (Cu) and Cu_5Zr solidify at approximately 970 °C with a phase fraction of 43.3 at.% and 35.7 at.%, respectively. The solidification path (Fig. 6(i)) of Alloy B5 is as follows: Liquid → Liquid + τ_3 → Liquid + τ_4 → Liquid + τ_4 + $Cu_{51}Zr_{14}$→ Liquid + τ_4 + $Cu_{51}Zr_{14}$ + (Cu). In Fig. 6(j), it can be found that the phase fractions for $Cu_{51}Zr_{14}$ and τ_4 are 82.5 at.% and 0.6 at.%, respectively.

By analyzing the as-cast microstructures and solidification paths of the alloys, it is obvious that they have different phases, which will affect their properties [26,27]. As a result, the friction and wear experiments were conducted in the present work to understand the effect of solidification structure on the wear resistance for the designed alloys.

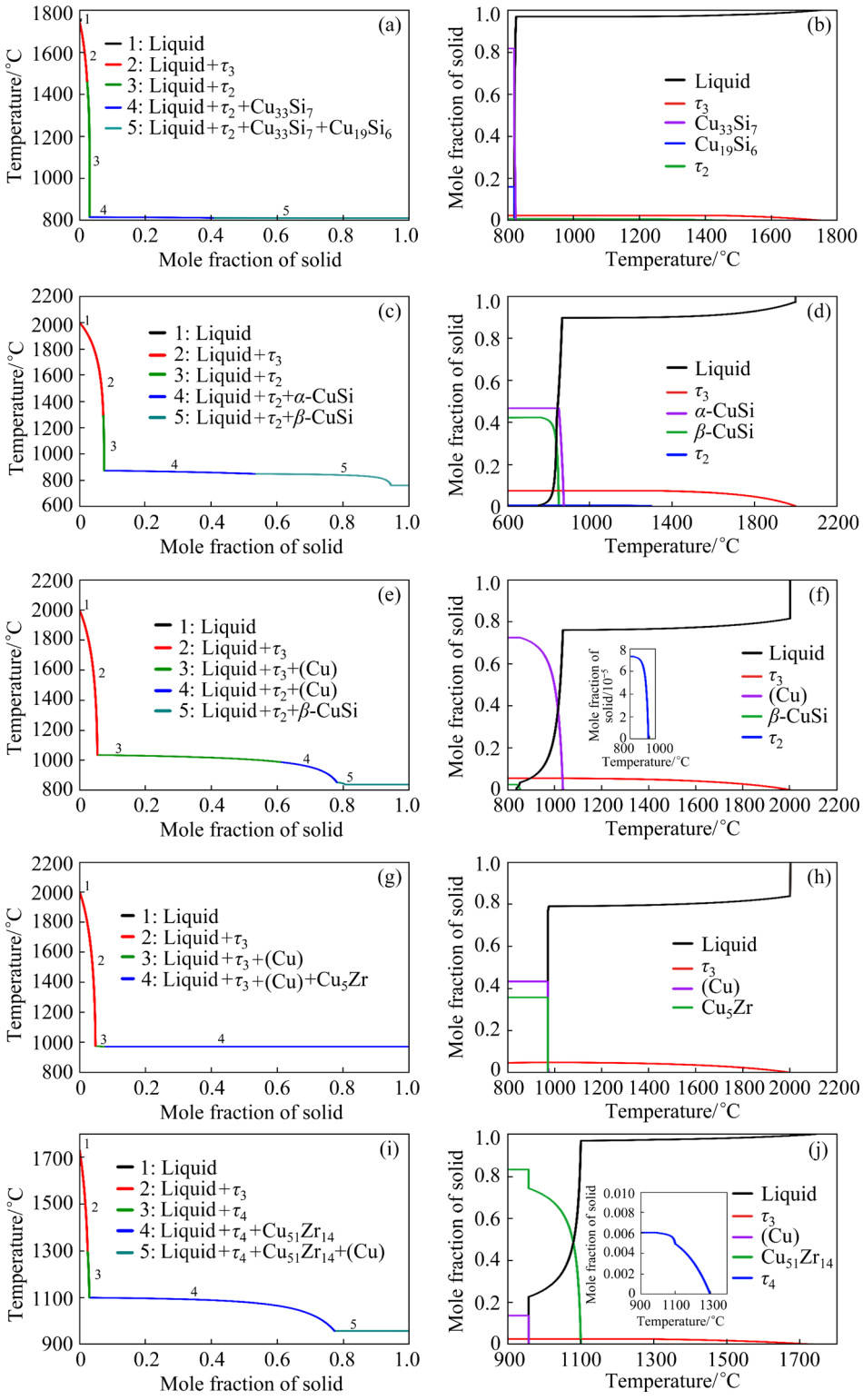

Fig. 6 Calculated Scheil−Gulliver solidification curves and mole fractions of phases vs temperature for different alloys: (a, b) Alloy B1 ($Cu_{80}Zr_1Si_{19}$); (c, d) Alloy B2 ($Cu_{80}Zr_4Si_{16}$); (e, f) Alloy B3 ($Cu_{80}Zr_8Si_{12}$); (g, h) Alloy B4 ($Cu_{80}Zr_{13}Si_7$); (i, j) Alloy B5 ($Cu_{80}Zr_{19}Si_1$)

3.4 Vickers hardness and coefficient of friction (COF)

The Vickers hardness of each alloy was tested at five different positions and the results are shown in Fig. 7(a). It is clear that Alloy B1 has the maximum average hardness (HV 496), followed by Alloy B5 (HV 342), whereas Alloy B3 possesses the minimum value (HV 161), which are listed in

Table 5. Figure 7(b) presents the micrographs of the indentation at different locations for the five alloys.

Under the dry friction condition, the tribological behavior of a material is primarily influenced by the friction load and speed which are 100 N and 200 r/min, respectively, in the present work. Test specimens were prepared as cylinders with a diameter of 5 mm. The measured COF and wear rate are summarized in Table 5, and the COF vs time curves are shown in Fig. 8. The variation trend of the COF curves for Alloys B1−B5 is similar. Firstly, the COF increases rapidly but it then fluctuates in a range as the wear time progresses because the wear debris is not removed from the friction area. Since the friction heat generated between the friction partner and the alloy sample during the friction process acts as the lubricant, the COF tends to remain unchanged during the last friction periods. Under the present testing condition, the COF values for Alloys B1−B5 are 0.20, 0.25, 0.27, 0.26 and 0.23, respectively.

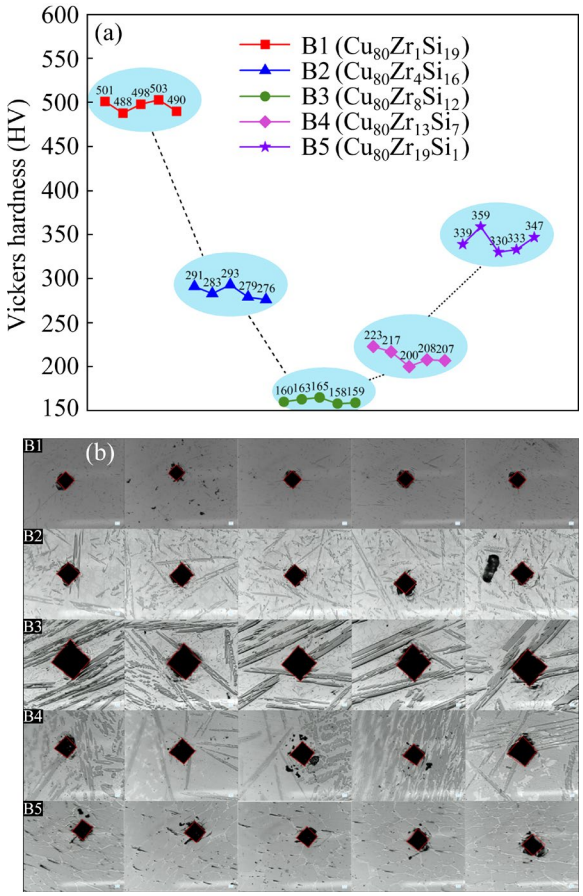

Fig. 7 Vickers hardness (a) and micrographs (b) of Alloys B1−B5 at different positions

Table 5 Average hardness and friction wear results for Alloys B1−B5

Alloy	Average hardness (HV)	COF	Wear rate/ (10^{-7}mm^3·N^{-1}·m^{-1})
B1	496	0.2	2.72
B2	285	0.25	2.77
B3	161	0.27	4.41
B4	211	0.26	3.35
B5	342	0.23	2.19

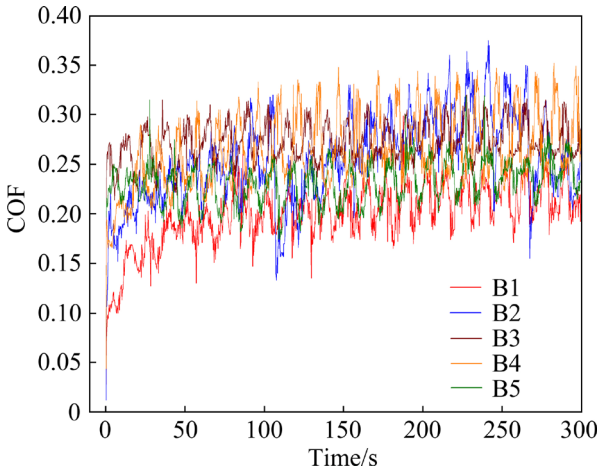

Fig. 8 COF as function of time for Alloys B1−B5 under dry friction

The wear rate of the alloys was calculated using Eq. (2) by measuring the mass before and after wear. The obtained results are listed in Table 5. Figure 9 shows the values of the COF and wear rate for the designed alloys. It demonstrates that both the COF and wear rate initially increase and then decrease. Accordingly, Alloy B5 exhibits the smallest wear rate and Alloy B3 exhibits the largest wear rate, with the values of 2.19 and 4.41×10^{-7} mm^3/(N·m), respectively.

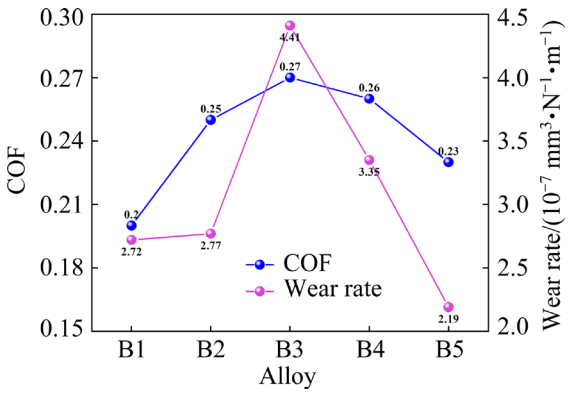

Fig. 9 COF and wear rate of Alloys B1−B5

3.5 Wear mechanism

The morphologies of the wear surfaces were analyzed based on the calculation of phase compositions, solidification paths and phase fractions using the CALPHAD method. The wear mechanism was then revealed. Figure 10 presents SEM micrographs of the wear surfaces. Under the dry friction condition, the wear mechanism is mainly adhesive and oxidative wear.

The SEM micrographs of Alloy B1 after wear are shown in Figs. 10(a, c). The areas with wear characteristics were selected for more detailed

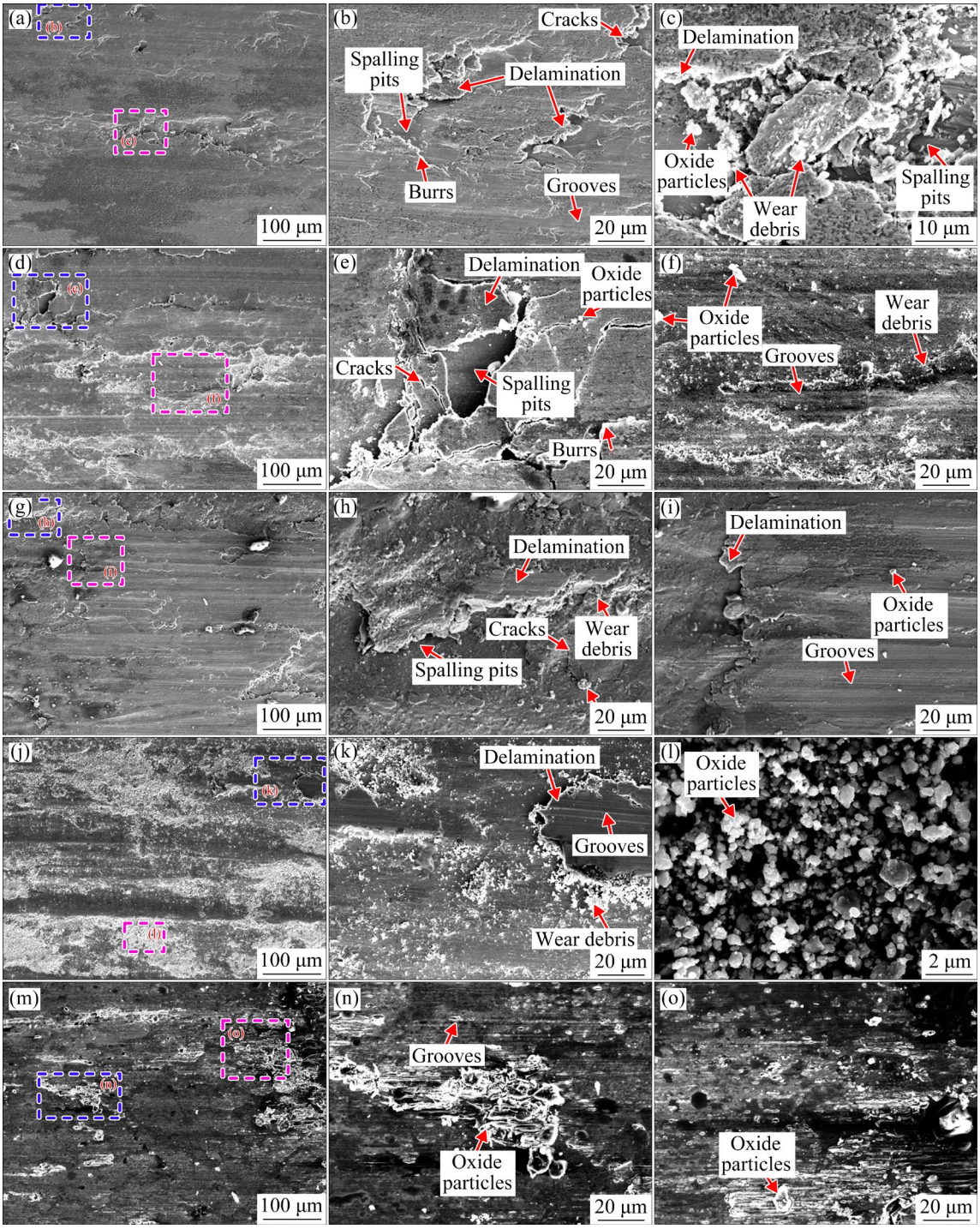

Fig. 10 SEM micrographs of wear surface of alloys: (a−c) Alloy B1 ($Cu_{80}Zr_1Si_{19}$); (d−f) Alloy B2 ($Cu_{80}Zr_4Si_{16}$); (g−i) Alloy B3 ($Cu_{80}Zr_8Si_{12}$); (j−l) Alloy B4 ($Cu_{80}Zr_{13}Si_7$); (m−o) Alloy B5 ($Cu_{80}Zr_{19}Si_1$) (The first micrograph shows the wear surface morphology of the alloy; The second one (blue region) and third one (purple region) are enlargements of the first one)

analysis. It can be seen from Fig. 10(b) that, there exist grooves, delamination and burrs on the wear surface. Due to the low surface hardness of the alloys compared to the friction pair, the high-speed rotation and pressure lead to the destruction of the surface layer. A partial magnification of the surface (Fig. 10(c)) shows that the depression is surrounded by spalling wear debris and oxide particles. The spalling pits are formed by some of the wear debris being peeled off, while the oxide particles are formed by the wear debris in contact with air. The oxide particles adhered to the surface provide the lubrication and thus reduce the COF. Similarly, the wear surfaces of Alloys B2−B4 also contain grooves, oxide particles and spalling pits. By contrast, only grooves and oxide particles are present on the wear surfaces (Figs. 10(m−o)) of Alloy B5. Additionally, its surface is blackened due to the heat generated by friction. The above observation suggests that the wear of Alloy B1 is severer than that of Alloy B5.

As described in Section 3.3, the fibrous ternary phases σ and τ_3 can be found in Alloys B1−B3. They are mostly in the form of sharp fine fibers in Alloys B1 and B2, which can lead to stress concentration and reduce the strength of the alloys. By contrast, there are more elongated fiber structures in Alloy B3, which lead to the delamination during friction and thus increase the wear rate. Therefore, Alloys B1−B3 will wear more severely during the friction and the ternary phases σ and τ_3 are poorly wear-resistant. The solidification micrographs of Alloy B4 show elongated ternary phase τ_3, with some of these fibers interconnected and disordered. During the friction, flake fibers that are oriented in the same direction tend to delaminate and the disordered fibers lead to the formation of more oxide particles. It is further elucidated that the wear resistance of the ternary compound τ_3 is poor. No ternary compound is detected in the solidification micrographs of Alloy B5. According to the elemental mapping, the distributions of Cu, Zr and Si are homogeneous. The addition of a small amount of Si refines the microstructure and improves the strength of the alloy. Therefore, the wear of Alloy B5 during friction is relatively light. The composition of the alloy should be controlled reasonably to avoid the precipitation of the τ_3 phase, which will deteriorate the properties.

Table 6 lists the element contents of Alloys B1−B5 before and after wear. The EDS results of Alloys B1−B5 before and after wear are also compared, as shown in Fig. 11. It can be seen that the elements O, C and Fe are attached to the surface after wear. The highest content of C (30 at.%−40 at.%) indicates that the abrasive particles of the friction are attached to the surface of the specimen during the friction process. The O content ranges from 10 at.% to 20 at.%, which is related to the production of oxide particles on the wear surface. Additionally, trace amount of Fe is attached to the wear surface. EDS analysis was conducted on various wear regions of Alloy B1, as shown in Figs. 12(a) and (b). The presence of more O and a small amount of Fe within Regions 1 and 5 indicates that more oxides are attached to the surface. Conversely, Regions 2, 4, and 6 exhibit high Cu content and low O content, indicating the possibility of delamination and less oxides in these regions. Specifically, the element content of Region 2 is Cu−0.9Zr−3.9Si−2.3O (at.%). EDS analysis was conducted on various regions of the wear surface for Alloy B2 (Figs. 12(c) and (d)). High levels of O and C are detected in the wear region. This is consistent with the results observed in the SEM micrographs, which show a number of oxide particles adhered to the wear surface. An area measuring 1 mm × 1 mm on the wear surface of the sample was scanned using 3D Profiling. Figure 13 shows the surface and 3D morphologies of the alloys with spalling pits and grooves on the wear

Table 6 Elemental contents of alloys before and after wear

Condition	Alloy	Content/at.%					
		Cu	Zr	Si	O	C	Fe
Before wear	B1	79.4	1.7	18.9			
	B2	78.8	4.7	16.5			
	B3	75.0	10.0	15.0			
	B4	71.1	15.3	13.7			
	B5	79.9	18.9	1.2			
After wear	B1	43.4	1.6	8.1	16.6	29.9	0.4
	B2	34.7	0.5	7.2	23.9	33.1	0.6
	B3	37.6	3.8	5.7	12.7	40.0	0.2
	B4	49.8	5.9	2.9	10.5	30.7	0.2
	B5	38.7	8.9	0.4	16.4	35.6	−

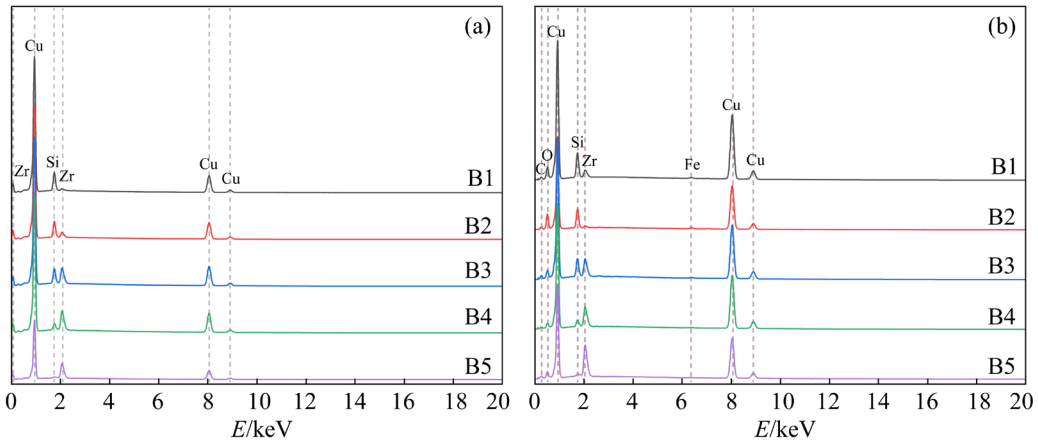

Fig. 11 EDS results of Alloys B1−B5 before (a) and after (b) wear

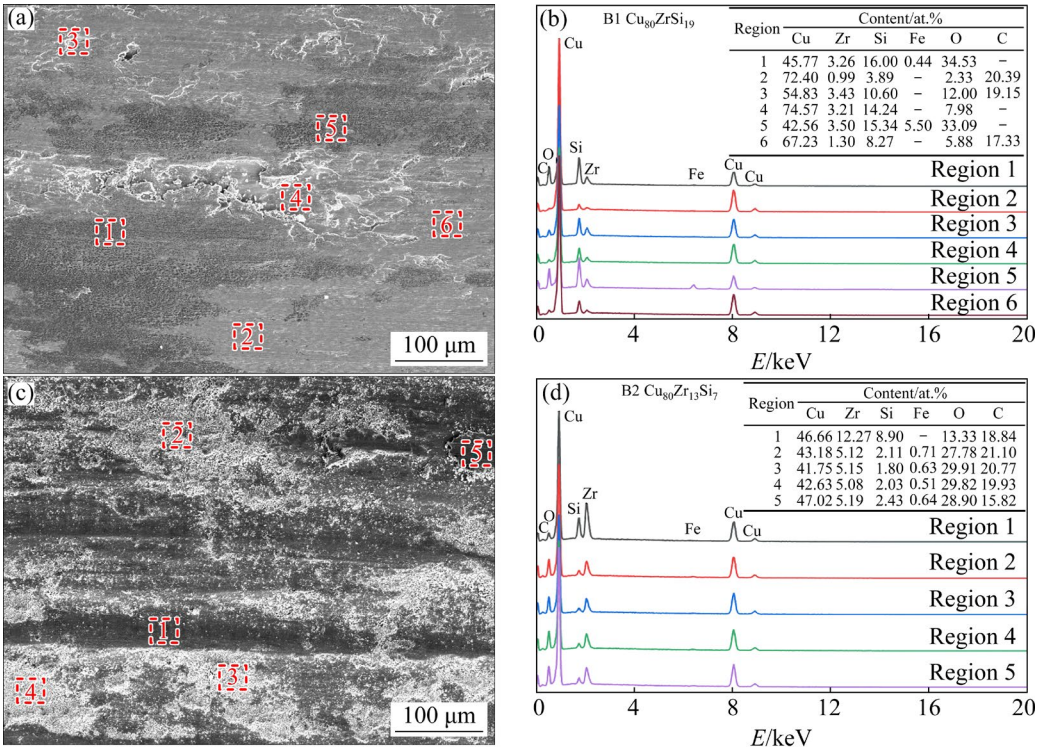

Fig. 12 Elemental contents in different areas of wear surface: (a, b) Alloy B1 ($Cu_{80}ZrSi_{19}$); (c, d) Alloy B2 ($Cu_{80}Zr_4Si_{16}$)

surface. The color from red to blue indicates the depth of the wear surface from low to high. The lower depth of wear is the spalling pit, which is more prominent in Alloys B1−B3, and the wear surface is flatter in Alloys B4 and B5.

Under the dry friction condition, the wear morphology of the alloy exhibits phenomena such as inhomogeneity, particle adhesion and dislodgement. However, the SEM micrographs in the present work mainly reveal grooves, wear debris and oxide particles and lack obvious features for plastic deformation. The analysis of the wear surface morphology of the alloys reveals that the main wear mechanisms of the Cu−Zr−Si alloy are adhesive and oxidative wear [6,28]. Observing the alloy wear morphology also suggests that the surface wear of Alloys B1, B2 and B3 is severer, while the wear surfaces of Alloys B4 and B5 contain more oxides. Alloy B1 exhibits the high hardness but suffers from significant brittleness, resulting in a considerable increase in wear during the friction and wear processes. After a comprehensive evaluation of properties, Alloy B5 ($Cu_{80}Zr_{19}Si_1$) demonstrates the best performance, similar to the Cu−Ni−Sn [2,29], Cu−Cr [8] and Cu−Ag−W [30] alloys.

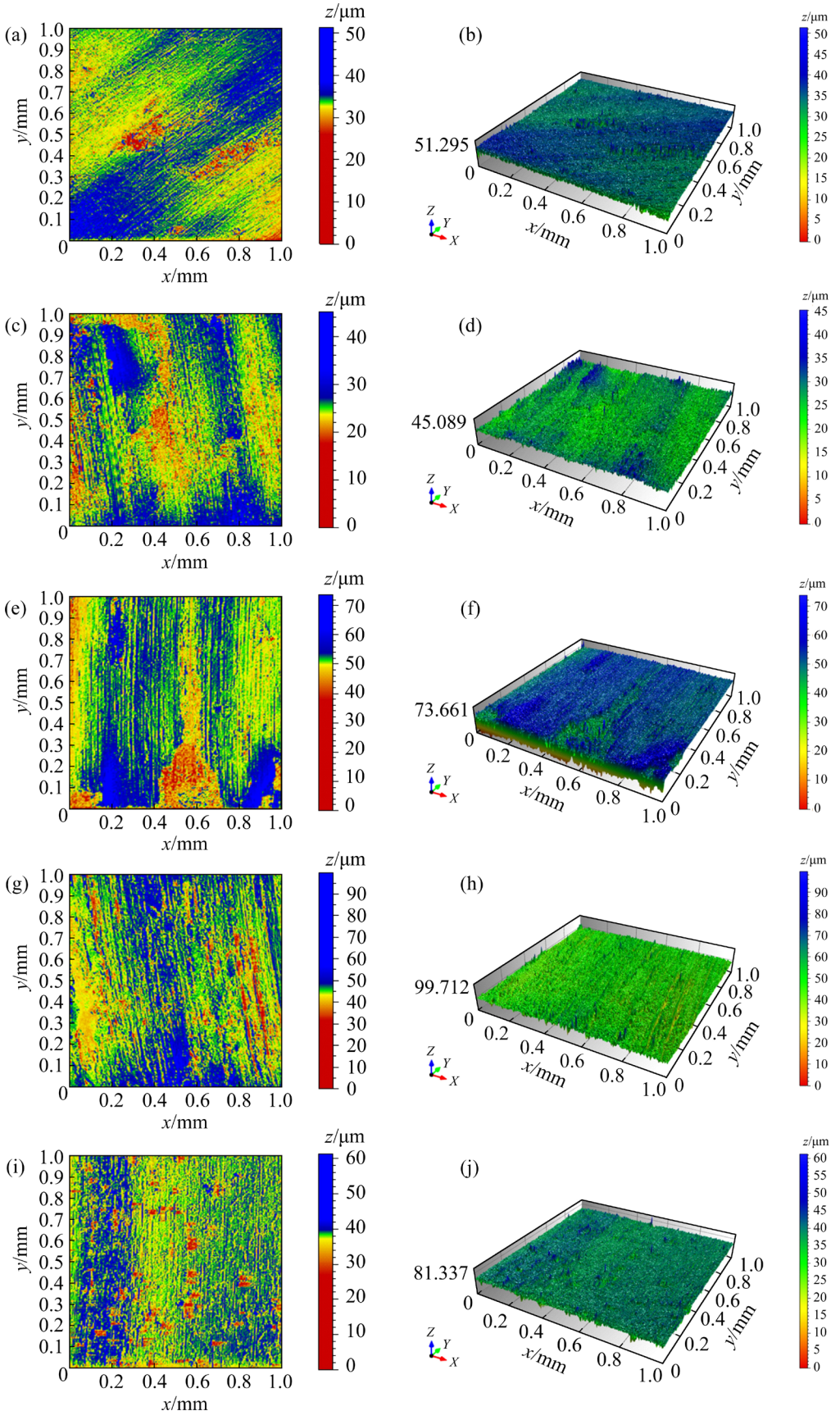

Fig. 13 Surface (a, c, e, g, i) and 3D (b, d, f, h, j) morphologies of alloys: (a, b) Alloy B1 ($Cu_{80}ZrSi_{19}$); (c, d) Alloy B2 ($Cu_{80}Zr_4Si_{16}$); (e, f) Alloy B3 ($Cu_{80}Zr_8Si_{12}$); (g, h) Alloy B4 ($Cu_{80}Zr_{13}Si_7$); (i, j) Alloy B5 ($Cu_{80}Zr_{19}Si$)

4 Conclusions

(1) The phase equilibria of the Cu−Zr−Si system at 600 °C were measured. Fourteen three-phase regions and two two-phase regions were determined. Four ternary compounds were confirmed.

(2) The thermodynamic assessment of the Cu−Zr−Si system was carried out based on the experimental data available in the literature and present work. A set of thermodynamic parameters were obtained. The calculated isothermal sections are in a good agreement with most of the experimental data.

(3) Five Cu−Zr−Si alloys were designed by the CALPHAD method and the microstructures of the alloys were analyzed by SEM−EDS. The Scheil−Gulliver solidification curves and step diagrams were obtained.

(4) Alloy B1 ($Cu_{80}Zr_1Si_{19}$) has the highest hardness value (HV 496), the lowest COF (0.2) and the wear rate of 2.72×10^{-7} $mm^3/(N\cdot m)$, followed by Alloy B5 ($Cu_{80}Zr_{19}Si_1$) with HV 342, 0.23 and 2.19×10^{-7} $mm^3/(N\cdot m)$, respectively.

(5) The wear mechanism is mainly adhesive and oxidative wear. The surface morphology after wear is composed of grooves, oxide particles and spalling pits. Considering the hardness, COF, wear rate and wear morphology, Alloy B5 ($Cu_{80}Zr_{19}Si_1$) exhibits the best overall mechanical performance.

CRediT authorship contribution statement

Ben-fu LI: Investigation, Formal analysis, Data curation, Writing − Original draft; **Biao HU:** Supervision, Project administration, Funding acquisition, Methodology, Resources, Writing − Review & editing; **Xin-yue HUANG:** Resources, Visualization, Formal analysis; **Rui ZUO:** Resources, Visualization, Formal analysis, Methodology; **Yu-ling LIU:** Methodology, Resources, Formal analysis; **Xin-yue LAN:** Supervision, Resources, Methodology; **Liang-yan HAO:** Writing – Review, Editing & polishing; **Wei XIONG:** Supervision, Methodology, Resources, Writing − Review & editing; **Rong-xun PIAO:** Supervision, Methodology, Resources.

Declaration of competing interest

The authors declare that they have no known competing financial interests or personal relationships that could have appeared to influence the work reported in this paper.

Acknowledgments

This work was supported from the Outstanding Youth Talents Fund in Anhui Provincial Colleges and Universities, China (No. 2023AH020027), the National Natural Science Foundation of China (No. 52071002), the University Synergy Innovation Program of Anhui Province, China (No. GXXT-2023-019), and the National Innovative Training Program for College Students, China (No. 202210361075).

References

[1] LIU Yu-ning, WANG Yun-peng, ZHU Ru-fei, WANG Hu, BAI Yi-ke, LOU Hua-fen. Research status and development trend of wear-resistant copper alloy [J]. Materials for Mechanical Engineering, 2021, 45(1): 1−7. (in Chinese)

[2] CHEN Kai-xuan, WU Xue-hua, ZHANG Ai-jun, ZHANG Jia-wei, CHEN Xiao-hua, ZHU Yu-zhi, WANG Zi-dong. Development of wear resistant Cu−12Sn−1.5Ni alloy via minor addition of Fe during casting process [J]. Applied Surface Science, 2022, 573: 151623.

[3] REN F, ARSHAD S N, BELLON P, AVERBACK R S, POURYAZDAN M, HAHN H. Sliding wear-induced chemical nanolayering in Cu−Ag, and its implications for high wear resistance [J]. Acta Materialia, 2014, 72: 148−158.

[4] ZHOU Shi-jie, TANG Sheng-yu. Study on wear resistance of complex aluminum brass for sliding bearing [J]. Special Casting & Nonferrous Alloys, 2005, 25(11): 699−701. (in Chinese)

[5] CAO Jun, SU Cheng-hao. Research status and development trend of Cu−Zr alloy [J]. Transactions of Materials and Heat Treatment, 2023, 44(5): 16−24. (in Chinese)

[6] WANG Wen-wei-jiao, ZHANG Yun-hao, YANG Hai-te, SU Long-shui, WANG Chen, TONG Chang-qing, ZHOU Jian-hui, CHEN Jun-feng, WANG Bing-shu. Effects of Si addition on properties and microstructure of CuCrZr alloy [J]. Journal of Alloys and Compounds, 2022, 906: 164277.

[7] LIAO Wan-neng, ZHANG Chen-xing, QIANG Hui, SONG Wei-fei, HU Yang-yang. The comprehensive performance and strengthening mechanism of the columnar crystal Cu−Ni−Si alloy after two large deformation rates of cryogenic rolling-aging [J]. Journal of Alloys and Compounds, 2023, 936: 168281.

[8] MA Ya-xing, QIAN Lei, CHENG Jin-juan, GAO Yang, MENG Xiang-peng, AGBEDOR S O, XIAO Zhu. Microstructure and properties of a Cu−6Cr alloy with high friction and wear resistance [J]. Wear, 2023, 514−515: 204553.

[9] DONG Zhi-li, TANG Xiang-yun, KU Mao-de. Mechanical Properties of highly conductive Cu−Zr−Si alloys [J]. Rare Metals, 1989, 13(5): 400−403. (in Chinese)

[10] LI Jian-wei, WONGSA-NGAM J, XU Jie, SHAN De-bin, GUO Bin, LANGDON T G. Langdon. Wear resistance of an ultrafine-grained Cu−Zr alloy processed by equal-channel angular pressing [J]. Wear, 2015, 326/327: 10−19.

[11] DU Yong, RAINER S F, WANG Jin-cheng, LIU Shu-hong, WANG Jian-chuan, JIN Zhan-peng. Computational design of engineering materials: Fundamentals and case studies [M]. Cambridge University Press, 2023.

[12] SPRENGER H. Die ternären systeme (titan, zirkonium,

hafnium)−kupfer−silizium [J]. Journal of the Less Common Metals, 1974, 34(1): 39−71.
[13] XIAO Meng, DU Yong, LIU Zhi-jian, XU Kai, CHEN Chong, QIU Lian-chang, ZHANG Hua-qing, LIU Yu-ling, LIU Shu-hong. Phase equilibria of the Cu−Zr−Si system at 750 and 900 °C [J]. Calphad, 2020, 68: 101727.
[14] DINSDALE A T. SGTE data for pure elements [J]. Calphad, 1991, 15(4): 317−425.
[15] LIU Yu-ling, LIU Shu-hong, ZHANG Cong, DU Yong, WANG Jiong, LI Yi-wei. Experimental investigation and thermodynamic description of the Cu−Zr system [J]. Journal of Phase Equilibria and Diffusion, 2017, 38: 121−134.
[16] YAN X Y, CHANG Y A. A thermodynamic analysis of the Cu−Si system [J]. Journal of Alloys and Compounds, 2000, 308(1): 221−229.
[17] GUENEAU C, SERVANT C, ANSARA I, DUPIN N. Thermodynamic assessment of the Si−Zr system [J]. Calphad, 1994, 18(3): 319−327.
[18] REDLICH O, KISTER A T. Thermodynamics of nonelectrolyte solutions-*x*−*y*−*t* relations in a binary system [J]. Industrial & Engineering Chemistry, 1948, 40(2): 341−345.
[19] SHI Yu-chao, ZHANG Jin, LI Ben-fu, ZENG Gang, JIN Cheng-gang, HU Biao, LAN Xin-yue, DU Yong. Experimental investigation and thermodynamic calculation of the Cu−Cr−Ti ternary system [J]. Calphad, 2023, 82: 102581.
[20] ZHOU Jia-qiang, HU Biao, LI Ben-fu, DU Yong, WANG Jiong. Experimental investigation and thermodynamic modeling of Cu−Nb−Si system [J]. Transactions of Nonferrous Metals Society of China, 2023, 33(3): 824−838.
[21] HU Biao, JIANG Yu, WANG Jiong, YAO Bin, MIN Fan-fei, DU Yong. Thermodynamic calculation of the T0 curve and metastable phase diagrams of the Ti−M (M = Mo, V, Nb, Cr, Al) binary systems [J]. Calphad, 2018, 62: 75−82.
[22] SUTTON D C, LIMBERT G, STEWART D, WOOD R J K. A functional form for wear depth of a ball and a flat surface [J]. Tribology Letters, 2014, 53: 173−179.
[23] PIERRE V, CALVERT L D, PEARSON W B. Pearson's handbook of crystallographic data for intermetallic phases [M]. New York: ASM International, 1986.
[24] SUNDMAN B, JANSSON B, ANDERSSON J O. The thermo-calc databank system [J]. Calphad, 1985, 9(2): 153−190.
[25] JIN Cheng-gang, HU Biao, ZENG Gang, XIE Jing, SHENG Shao-ding, LIU Shu-hong, HU Jie-qiong. Experimental investigation and CALPHAD modeling of phase equilibria of the Cu−Ag−Zr system [J]. Calphad, 2022, 79: 102487.
[26] LI Xiao-jing, LIU Shu-hong, DU Yong. Investigation on the corrosion resistance of the Mg−10Al−*x*Mn alloys based on thermodynamic calculations [J]. Corrosion Science, 2021, 189: 109631.
[27] ZENG Gang, HU Biao, SHI Yu-chao, LAN Xin-yue, YIN Hui-qin. Corrosion resistance investigation of the Ti−Al−Mo system supported by CALPHAD approach and key experiments [J]. Corrosion Science, 2024, 229: 111857.
[28] SHEKHAR C, WANI M F, SEHGAL R. Fabrication and self-lubricating tribological characterisation of Cu−Ni/TiC/CaF_2 composite for railway switch slide baseplate [J]. Wear, 2023, 526/527: 204890.
[29] XIAO Jin-kun, ZHANG Wei, LIU Li-ming, GAN Xue-ping, ZHOU Ke-chao, ZHANG Chao. Microstructure and tribological properties of plasma sprayed Cu−15Ni−8Sn coatings [J]. Surface and Coatings Technology, 2018, 337: 159−167.
[30] ZHU Wei-wei, ZHAN Can-can, KWOK C T, ZHOU Jian, REN Fu-zeng. Effects of nanocrystalline microstructure on the dry sliding wear behavior of a Cu−10 at.%Ag−10at.%W ternary alloy against stainless steel [J]. Wear, 2018, 402/403: 1−10.

Cu−Zr−Si 合金的相平衡和摩擦磨损机制

李奔富[1]，胡 标[1]，黄馨悦[1]，左 锐[1]，刘玉玲[1]，兰新月[1]，郝良彦[2]，熊 伟[2]，朴荣勋[3]

1. 安徽理工大学 材料科学与工程学院，淮南 232001；
2. Department of Mechanical Engineering and Materials Science, University of Pittsburgh, Pittsburgh 15261, USA；
3. 安徽理工大学 机械工程学院，淮南 232001

摘 要：采用 X 射线衍射和扫描电子显微镜及能量分散光谱对 Cu−Zr−Si 体系在 600 ℃的相平衡进行实验测定。采用相图计算方法进行热力学优化并获得一套准确描述 Cu−Zr−Si 体系的热力学参数。基于相图计算设计了 5 种铸态合金，采用 Scheil−Gulliver 模型对合金的凝固路径进行模拟。通过测试铸态合金的硬度和摩擦磨损性能，并结合扫描电镜和 3D 形貌仪对磨损形态的观察发现 $Cu_{80}Zr_{19}Si_1$ 合金具有良好的性能，其硬度为 HV 342、摩擦因数为 0.23、磨损率为 2.19×10^{-7} mm^3/(N·m)。磨损表面的主要特征是犁沟、剥落坑和氧化物颗粒。合金在干滑动条件下的磨损机制为黏着磨损和氧化磨损。本文研究工作为 Cu−Zr−Si 耐磨合金的设计提供了重要理论依据。

关键词：Cu−Zr−Si 合金；热力学建模；CALPHAD 方法；摩擦因数；磨损机制

(Edited by Wei-ping CHEN)